Digest Journal of
Nanomaterials and Biostructures

Dig. J. Nanomater. Bios. **2026**; 21(2): 55240
https://doi.org/10.31083/DJNB55240

Original Research

Ce-Doped $NiCo_2O_4$/Polyvinyl Alcohol/Reduced Graphene Oxide Composites: Synthesis, Characterization, and Electromagnetic Interference Shielding Effectiveness

Venkayamma U[1], Rajesh Babu B[2,*], Samatha K[1,*], S Jahnavi V[2]

[1]Department of Physics, Andhra University, 530003 Visakhapatnam, Andhra Pradesh, India
[2]Department of Physics, Gayatri Vidya Parishad College of Engineering for Women, 530048 Visakhapatnam, Andhra Pradesh, India
*Correspondence: rajeshbabu.bitra@gmail.com (Rajesh Babu B); samatha_k2002@yahoo.co.in (Samatha K)

Academic Editor: Karol Kyzioł
Submitted: 24 January 2026 Revised: 16 March 2026 Accepted: 1 April 2026 Published: 24 June 2026

Abstract

The structural, morphological, and magnetic properties of Ce-doped $NiCo_2O_4$ (Ce-$NiCo_2O_4$) spinel nanopowders synthesized via sol-gel autocombustion followed by annealing at 700 °C were systematically characterized using X-ray diffraction (XRD), Fourier transform infrared spectroscopy (FTIR), vibrating sample magnetometry, and scanning electron microscopy. XRD analysis revealed the formation of a single-phase cubic spinel structure with the $Fd3m$ space group. The introduction of Ce into the $NiCo_2O_4$ lattice increased the lattice parameter from 8.090 Å to 8.312 Å and reduced the crystallite size from 36 nm to 14 nm. Two prominent FTIR absorption bands were observed around 600 and 550 cm^{-1}, corresponding to octahedral and tetrahedral sites, respectively. A linear relationship between magnetization and applied field was observed, confirming the paramagnetic nature of all samples at room temperature. Ce-$NiCo_2O_4$ nanopowders were blended with polyvinyl alcohol (PVA) and reduced graphene oxide (rGO) to fabricate thick composite films for electromagnetic interference (EMI) shielding in the X-band frequency range (8–12 GHz). The synergistic combination of magnetic Ce-$NiCo_2O_4$ nanopowders, conductive rGO, and the flexible PVA matrix resulted in an enhanced EMI shielding performance. Our results suggest that Ce-$NiCo_2O_4$/PVA/rGO thick films are promising lightweight, flexible, and efficient EMI shielding materials for electronic and telecommunication applications.

Keywords: spinel oxide; XRD; VSM; electromagnetic shielding; microwave absorption

1. Introduction

$NiCo_2O_4$ (nickel cobaltite) nanoparticles have attracted considerable interest due to their unique spinel structure and superior electrochemical activity, electrical conductivity, and chemical stability, making them highly effective for applications in energy storage, catalysis, and environmental remediation [1]. Their mixed valence states of nickel and cobalt contribute synergistically to enhanced charge transport and catalytic properties compared to their single- metal oxide counterparts [2].

$NiCo_2O_4$ crystallizes in the spinel structure, which belongs to the cubic crystal system with space group $Fd\bar{3}m$. In this arrangement, oxygen anions form a close-packed face-centered cubic lattice, while nickel and cobalt cations occupy two different types of interstitial sites: tetrahedral (A) and octahedral (B). Typically, $NiCo_2O_4$ is considered an inverse spinel, where Ni^{2+} ions predominantly occupy the octahedral sites (B sites), while Co^{3+} ions are split between octahedral and tetrahedral positions, and Co^{2+} ions are usually found at the tetrahedral sites. The unique arrangement of cations in the $NiCo_2O_4$ (Fig. 1, Ref. [3]) results in distinctive electrical, magnetic, and electrochemical properties, making it a promising material for applications such as electrocatalysis, energy storage, and electromagnetic shielding.

To further improve the functional properties of $NiCo_2O_4$, numerous researchers modified $NiCo_2O_4$, by doping with rare-earth elements. The addition of rare earth elements, with a larger ionic radius, into the spinel lattice induces phase transformations and generates new phases that alter the material's properties. In particular, magnetic properties in cerium- doped ferrites are significantly influenced by interactions between Ce and Fe ions, attributable to the high angular momentum and unpaired 4f electrons of Ce^{3+} ions. Cerium typically exhibits a zero-oxidation state with the electron configuration $[Xe]4f^1 5d^1 6s^2$, which changes to $[Xe]4f^2 5d^0 6s^0$ upon oxidation to Ce^{2+}. However, the unstable Ce^{2+} state tends to stabilize as Ce^{3+} with a configuration of $[Xe]4f^1 5d^0 6s^0$. The strong 4f-3d coupling between Ce^{3+} and Fe ions markedly modifies Ce-Fe interactions [4,5]. Ferroelectric and ferromagnetic behaviors arise from the spin interactions of 3d electrons during Fe–Fe coupling, while the partial substitution of Fe^{3+} by rare earth ions (4f elements) generates 3d-4f coupling, facilitating electron hopping that governs these magnetic properties in spinel ferrites. Saturation magnetization decreases with increased substitution of non-magnetic Ce^{3+} ions in the octahedral sites, displacing some Fe^{3+} (5 µB) ions from tetrahedral sites to octahedral ones [6,7]. Despite Ce^{3+} possessing a magnetic moment (2.54 µB) larger than that of

---

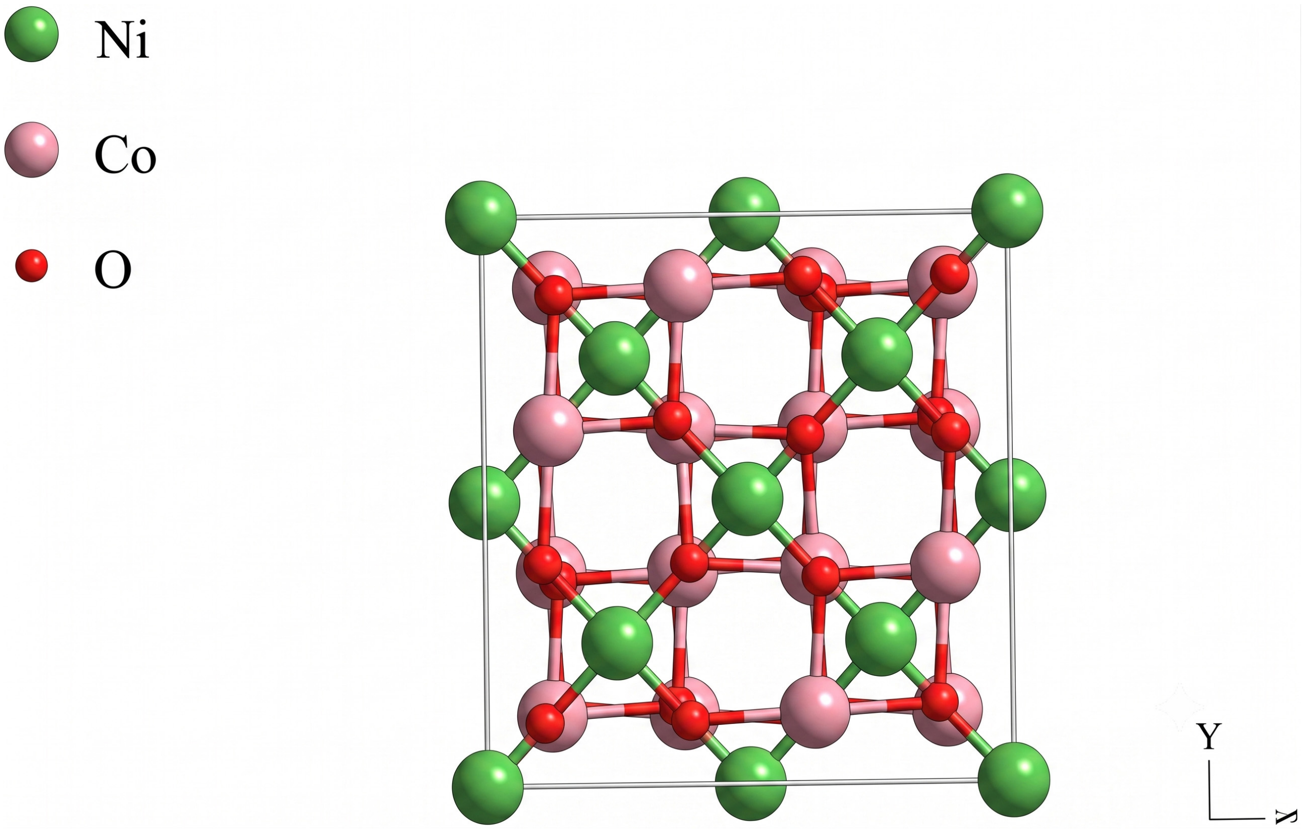

Fig. 1. Structure of $NiCo_2O_4$ spinel oxide [3].

Zn^{2+} (0 μB), Ce^{3+} shifts toward the tetrahedral site, and co-doping concentration leads to an overall increase [8,9]. The preference of Ce to occupy octahedral B-sites causes Fe^{3+} ions to move to A-sites, creating internal strain, expanding the lattice parameter, and causing lattice deformation [10].

Beyond magnetic applications, cerium nanoparticles also exhibit effective antibacterial activity through reversible redox transitions between Ce^{3+} and Ce^{4+} states, offering potent antimicrobial performance with lower toxicity [11]. Cerium oxide nanoparticles are distinguished by their dynamic redox behavior, easily transitioning between Ce^{3+} and Ce^{4+} oxidation states. This reversible redox cycling facilitates the formation of oxygen vacancies and active sites, thereby enhancing catalytic, antioxidant, and antimicrobial activities. Their unique cubic fluorite structure and nanoscale surface properties enable enzyme-like functions that can mitigate oxidative stress and promote catalytic reactions. Consequently, cerium nanoparticles exhibit significant potential in biomedical and environmental applications, demonstrating strong antibacterial efficacy while maintaining relatively low toxicity [5,12]. The Ce^{3+}-substituted Zn-ferrites exhibit reasonable microwave absorption due to their combination of high saturation magnetization and low coercivity [11,13]. Additionally, cerium-doped $NiCo_2O_4$ materials display refined particle morphologies and reduced grain sizes, leading to increased surface areas and enhanced reactivity [14,15].

Despite numerous studies on $NiCo_2O_4$ spinel oxides and polyvinyl alcohol (PVA)/reduced graphene oxide (rGO) composites separately, limited research has been conducted on the integration of Ce-doped $NiCo_2O_4$ nanopowders with PVA/rGO matrices for electromagnetic interference (EMI) shielding applications. The synergistic combination of magnetic spinel oxides with conductive graphene derivatives in a flexible polymer matrix is expected to provide superior EMI shielding performance through complementary absorption mechanisms.

In this study, we report the synthesis of Ce-doped $NiCo_2O_4$ spinel oxide nanopowders using a sol-gel auto combustion method followed by calcination at 700 °C. The present composition $Ce_xNiCo_{2-x}O_4$ ($x = 0.0, 0.05, 0.1$) was chosen in such a way that of Cobalt ions are possibly replaced by Cerium ions. While the differing oxidation states of Ce (3+, 4+) and Co (2+, 3+) present a potential for charge imbalance, the stoichiometry was maintained by assuming Ce^{3+} replaces Co^{3+} ions, with any excess charge from Ce^{4+} being balanced by the intrinsic mixed-valence nature of the Ni/Co cations and the formation of oxygen vacancies during the high-temperature calcination at 700 °C. The structural, morphological, optical, and magnetic properties of the synthesized nanopowders were investigated. Subsequently, the Ce-doped $NiCo_2O_4$ nanopowders were integrated with PVA and rGO to fabricate thick film composites, which were characterized for their EMI shielding

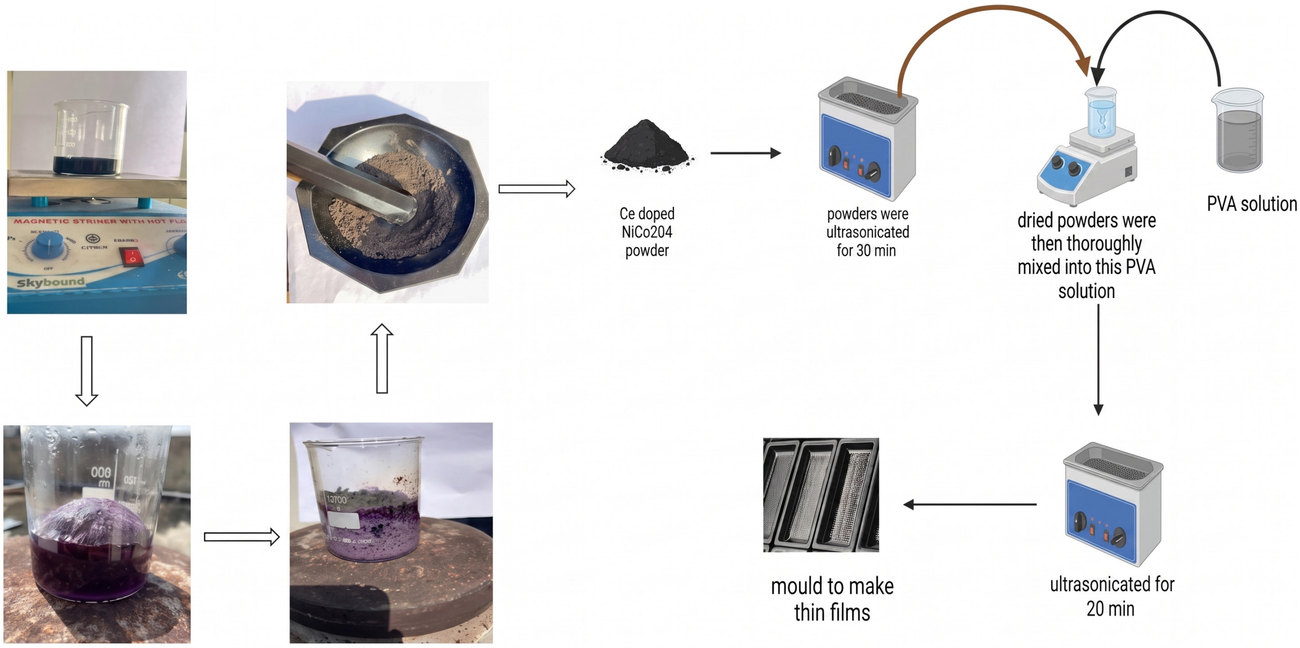

Fig. 2. Schematic representation of the synthesis of Ce-substituted $NiCo_2O_4$ nanoparticles and fabrication of thick composite films.

performance using vector network analyzer measurements. The effects of cerium doping on the spinel structure and contributions of magnetic nanopowders, rGO, and PVA to EMI shielding mechanisms are systematically discussed.

2. Materials and Methods

2.1 Synthesis of $Ce_xNiCo_{2-x}O_4$ Nanoparticles

The stoichiometric amounts of cobalt nitrate hexahydrate $Co(NO_3)_2 \cdot 6H_2O$ (Merck, New Delhi, India), nickel nitrate hexahydrate $Ni(NO_3)_2 \cdot 6H_2O$ (Merck), and cerium nitrate hexahydrate $Ce(NO_3)_3 \cdot 6H_2O$ (Merck) are used without any further purification to synthesize $Ce_xNiCo_{2-x}O_4$ ($x = 0.0, 0.05, 0.1$) nanoparticles. The individual metal nitrates were weighed and stirred continuously for one hour by mixing the required amount of metal nitrates in a minimum amount of deionized water and ethanol to obtain a clear solution. Further, citric acid ($C_6H_8O_7$, Merck) was added to the above metal nitrate mixture in the ratio 1:1 to act as a chelating agent (molar ratio of metal nitrate mixture to citric acid) at 70 °C temperature, and a few drops of NH_4OH solution were added to maintain the pH at 7. Further, the solution was gradually converted into a thick, brown, viscous gel, and with time, the gel self-ignited and a grey-colored ash was obtained. The Schematic procedure of synthesis and making thick composite films is demonstrated in Fig. 2.

2.2 Fabrication of Ce-$NiCo_2O_4$/PVA/rGO Thick Films

PVA was dissolved in deionized water at 80 °C under continuous stirring for 1 hour to obtain a homogeneous PVA solution. Graphene oxide was dispersed in deionized water using ultrasonication for 30 min to ensure uniform dispersion. The rGO dispersion was then mixed with the PVA solution under magnetic stirring. Appropriate amounts of Ce-doped $NiCo_2O_4$ nanopowders were ultrasonicated 30 min in ethanol medium and dried. Later, these dried powders were added to the PVA/rGO mixture and ultrasonicated for 20 min, followed by magnetic stirring for 15 min to achieve uniform distribution of the nanofiller in the polymer matrix. The resulting suspension was cast onto glass substrates and dried at room temperature for 24 hours and obtain free-standing thick films.

2.3 Characterization Techniques

The synthesized samples were characterized utilizing a Bruker (D8-Advance) x-ray diffractometer (Bruker Corp., Billerica, MA, USA) with a Cu-Kα radiation source ($\lambda = 1.5405$ Å) for phase analysis in the range of 10° to 90° at a scanning rate of 0.05°/min. Using a TESCAN MIRA (Brno, Czech Republic) scanning electron microscopy (SEM), pictures of scanning electron microscopy and energy dispersive spectroscopy were captured. To investigate vibrational modes of metal–oxygen bond, the Fourier transform infrared (FTIR) spectroscopy in the wavenumber range of 400–4000 cm^{-1} was studied using a Shimadzu IR Prestige-21 FTIR Spectrophotometer (Kyoto, Japan) with KBr pellets. Magnetic measurements were performed using a Vibrating Sample Magnetometer (VSM) module in a Physical Property Measurement System (PPMS, Quantum Design) at room temperature with a maximum applied field of ±20 kOe. The electromagnetic interference shielding effectiveness of the composite films was measured using a vector network analyzer (VNA) Keysight PNA/ENA equipped

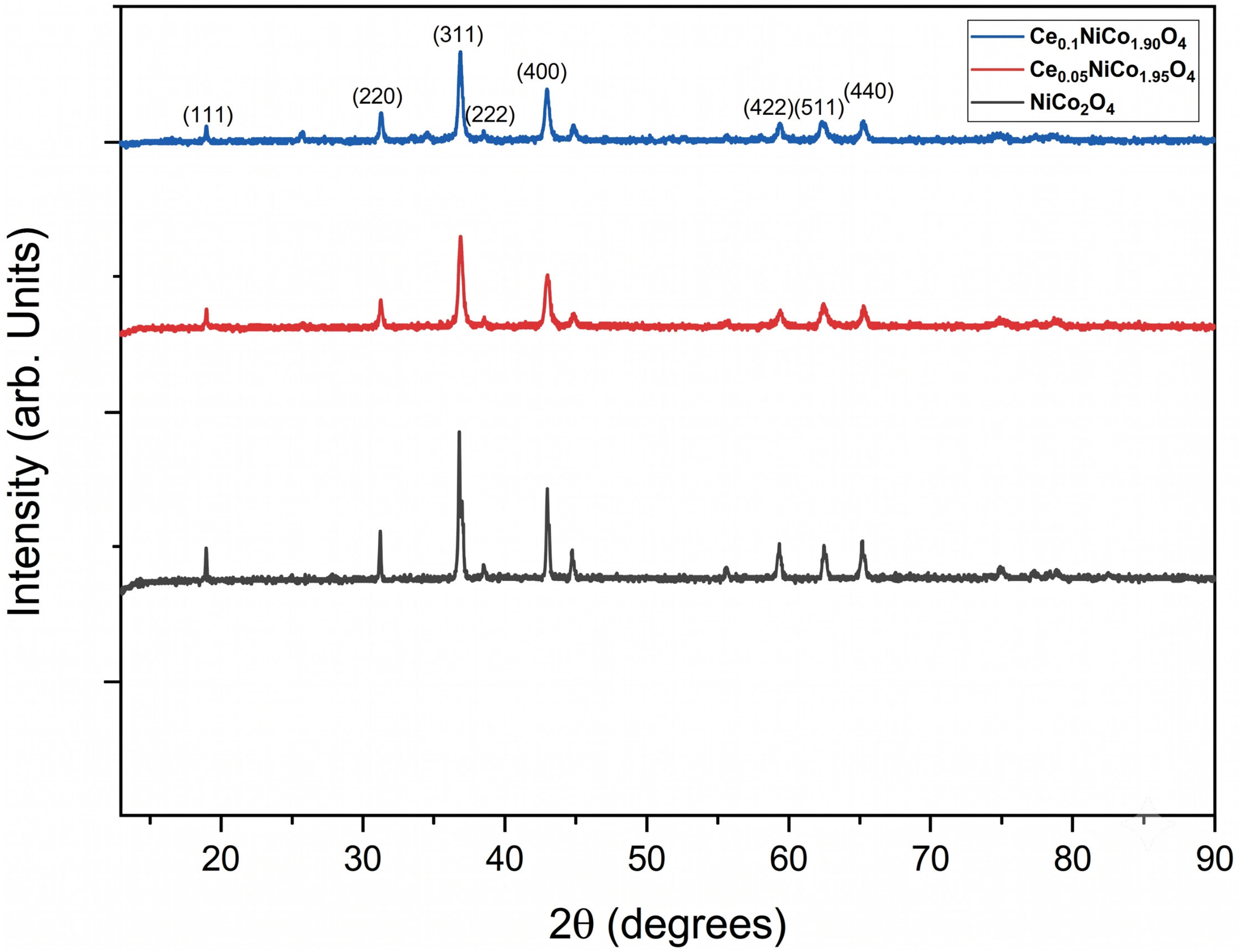

Fig. 3. X-ray diffraction patterns of Ce-substituted $NiCo_2O_4$ spinel oxide.

(Keysight Technologies, Inc., Santa Rosa, CA, USA) with waveguide adapters in the frequency range of 8–12 GHz (X-band).

3. Results

3.1 Structural Properties

X-ray diffraction patterns of the undoped $NiCo_2O_4$ and Ce-doped spinel oxides ($Ce_{0.05}NiCo_{1.95}O_4$ and $Ce_{0.1}NiCo_{1.9}O_4$) are presented in Fig. 3. The diffraction peaks observed at 2θ values around 18°, 31°, 36°, 38°, 44°, 55°, 59°, and 65° correspond to the (111), (220), (311), (222), (400), (422), (511), and (440) planes, respectively. These peaks match well with the cubic spinel structure of $NiCo_2O_4$ (Joint Committee on Powder Diffraction Standards (JCPDS) card no. 20-0781), confirming the successful formation of the inverse spinel phase [16,17].

Lattice Constant and Crystallite Size

The experimental lattice constant was determined by using standard Bragg's equation and listed in Table 1 [18].

$$a_{expt} = d\left(\sqrt{h^2+k^2+l^2}\right) \tag{1}$$

where (h, k, l) represent the Miller indices corresponding to the crystal planes interacting with the x-rays. The average size of the crystallites (D) was determined by analyzing the broadening of the peaks in the X-ray diffraction (XRD) patterns using two methods: the Debye-Scherrer equation (Eqn. 2) and the Williamson-Hall (W-H) method Eqn. 3 [19,20].

$$D_{311} = \frac{k\lambda}{\beta cos\theta} \tag{2}$$

where 'k' is the shape factor (usually 0.9), 'λ' represents the wavelength of the x-ray source (Cu-Kα radiation), and the peak width at half maximum intensity (FWHM) is measured in radians. Since the broadening of XRD peaks (FWHM) can be influenced by various factors like the instrument and internal strain within the crystal lattice (micro strain), the Williamson-Hall method was also used to estimate the average crystallite size.

Table 1. Composition (x), lattice constant (aexp), volume, density (D_x) and crystallite size of Ce-doped $NiCo_{2-x}O_4$ spinel oxide.

	Lattice		X-ray	Crystallite size (nm)	
Composition	constant	constant	constant	D_{311}	W-H method
Ce (x)	a_{exp} (Å)	(Å)^3	g/cc		
0	8.090	529.7	3.1	36	13
0.05	8.125	536.3	2.9	20	18
0.1	8.312	574.2	2.7	14	16

$$\frac{\beta\cos\theta}{\lambda} = \frac{1}{D} + \frac{4\varepsilon\sin\theta}{\lambda} \tag{3}$$

This method takes into account both crystallite size and micro-strain effects, providing a complete and more accurate estimate of the crystallite. The calculated crystallite sizes are listed in Table 1.

3.2 Infrared Spectra Studies

Fig. 4 shows characteristic vibrational modes of Ce-doped $NiCo_2O_4$ nanoparticles and their compositional variations in the range 400 cm^{-1} to about 1200 cm^{-1}. These bands at ~550 cm^{-1} and ~600 cm^{-1} are assigned to the metal–oxygen (M–O) vibrations typical of spinel structures [21].

3.3 Surface Morphology and Grain Size Analysis

Fig. 5 shows Scanning electron microscope images of Ce-doped $NiCo_2O_4$ spinel oxide nanoparticles. It is clear that all the samples exhibit irregular morphology, which is typical for materials synthesized via the sol-gel auto-combustion method. The elemental composition and stoichiometric purity of the synthesized Ce-doped $NiCo_{2-x}O_4$ nanoparticles were verified using Energy Dispersive X-ray (EDX) analysis.

3.4 Magnetic Properties

Fig. 6 shows the room-temperature magnetization versus applied magnetic field of Ce-doped $NiCo_2O_4$ spinel oxide nanopowders. As evident from the figure, all samples show magnetization (M) as a function of applied field (H) passing through the origin, indicating a linear relation that is typical of paramagnetic materials.

3.5 EMI Shielding Performance

The electromagnetic interference shielding effectiveness of Ce-doped $NiCo_2O_4$/PVA/rGO composite films was evaluated using vector network analyzer measurements in the X-band frequency range (8–12 GHz) are shown in Fig. 7. The total shielding effectiveness (SE_T) and its components, reflection loss (SE_R) and absorption loss (SE_A), were calculated from the measured scattering parameters (S_{11} and S_{21}) using standard [22]:

$$SE_T = -10log_{10}\left(P_T/P_I\right) = -10log_{10}\mid S_{21}\mid^2 \tag{4}$$

$$SE_R = -10log_{10}\left(1-\mid S_{11}\mid^2\right) \tag{5}$$

$$SE_A = -10log_{10}\left(\mid S_{21}\mid^2/\left(1-\mid S_{11}\mid^2\right)\right) \tag{6}$$

where P_I and P_T are the incident and transmitted power, respectively.

4. Discussion

4.1 Structural Analysis

All samples, including those doped with Cerium, preserve the spinel crystalline structure with no additional peaks, indicating that Ce doping does not introduce secondary phases or impurities. This suggests that Cerium ions are incorporated into the $NiCo_2O_4$ lattice sites without altering the fundamental crystal structure. The peak intensities for the (311) and (400) reflections decrease marginally with increasing Ce concentration, indicating a slight reduction in long-range crystallinity. The absence of additional peaks confirms the phase purity of the doped nanoparticles, essential for consistent magnetic and electronic properties. The calcination temperature of 700 °C was selected to achieve high crystallinity and complete phase formation of the spinel structure while ensuring the removal of all organic precursors from the sol-gel process. This temperature is critical for ensuring that Ce ions are successfully diffused into the $NiCo_2O_4$ host lattice without the segregation of CeO_2. To provide a quantitative assessment of the structural modifications, the peak intensity ratios for the most prominent reflections were analysed. The intensity of the (311) peak was compared against the (220) and (440) peaks and listed in Table 2. For the pure $NiCo_2O_4$ sample, the I_{311}/I_{220} ratio was determined to be 1.52 and the I_{311}/I_{440} ratio was 1.61. Upon Ce doping at x = 0.05, these ratios were calculated as 1.51 and 1.63, respectively. However, at the higher doping level of x = 0.1, a significant shift was observed, with the I_{311}/I_{220} ratio increasing to 2.38 and the I_{311}/I_{440} ratio reaching 2.26. This pronounced change in the

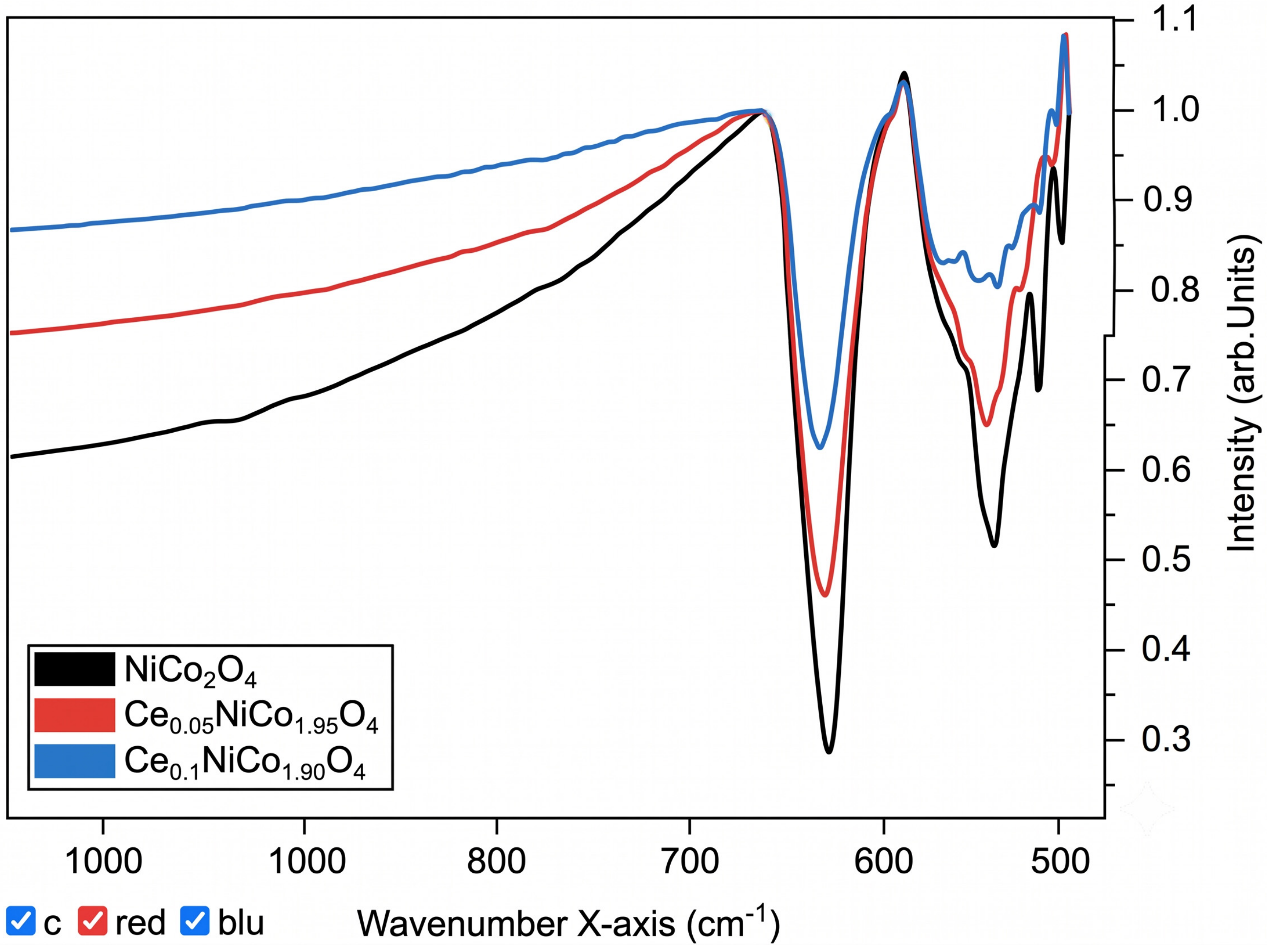

Fig. 4. FTIR spectra of Ce-substituted NiCo$_2$O$_4$ spinel oxide nanoparticles. FTIR, Fourier transform infrared spectroscopy.

relative intensities of the diffraction planes confirms that the incorporation of Ce ions—which exhibit a significant shift toward lower 2θ values due to lattice expansion—results in a redistribution of the host Ni and Co cations. These results are in strong agreement with the FTIR data, indicating that the substitution-induced strain alters the structure factor of the spinel lattice by favouring Ce occupancy in the larger octahedral B-sites.

Table 2. XRD peak ratios of Ce-doped NiCo$_2$O$_4$.

Composition (x)	I_{311}/I_{220}	I_{311}/I_{440}
0.00	1.52	1.61
0.05	1.51	1.63
0.10	2.38	2.26

XRD, X-ray diffraction.

Lattice Constant and Crystallite Size

It was found that (Table 2) the lattice constant increases as the dopant concentration Ce rises. This systematic rise in lattice constant with Ce content is consistent with Vegard's law, where the lattice constant varies linearly with the ionic radii of the substituent cations and their concentration. In the present work, a larger ionic radius of Ce^{3+} (1.01 Å) replacing Co^{3+} (0.6 Å) internal strain and lattice deformation, which accounts for the shift in XRD peaks toward lower values. The stability of the single-phase cubic spinel structure, as confirmed by XRD, indicates that the lattice accommodates Ce ions without modifying spinel phase. The charge neutrality in the Ce -doped system is likely governed by the transition of Ni^{3+} to Ni^{2+} or through the generation of oxygen vacancies. These vacancies not only assist in charge compensation but also contribute to the lattice expansion (from 8.090 Å to 8.312 Å) observed in Table 1. The substitution of larger Ce^{3+} ions (1.01 Å) for smaller Co^{3+} ions (0.60 Å) introduces lattice strain and local distortion within the spinel lattice. These structural perturbations hinder atomic diffusion and grain growth during the combustion and subsequent heat-treatment process. As a result, nucleation dominates over grain coarsening, leading to smaller crystallites. Furthermore, the citric acid to metal nitrate molar ratio (1:1) was optimized to control the combustion enthalpy. This environment promotes rapid nucleation, while the presence of larger Ce ions at the grain boundaries acts as a pinning agent, effectively inhibiting

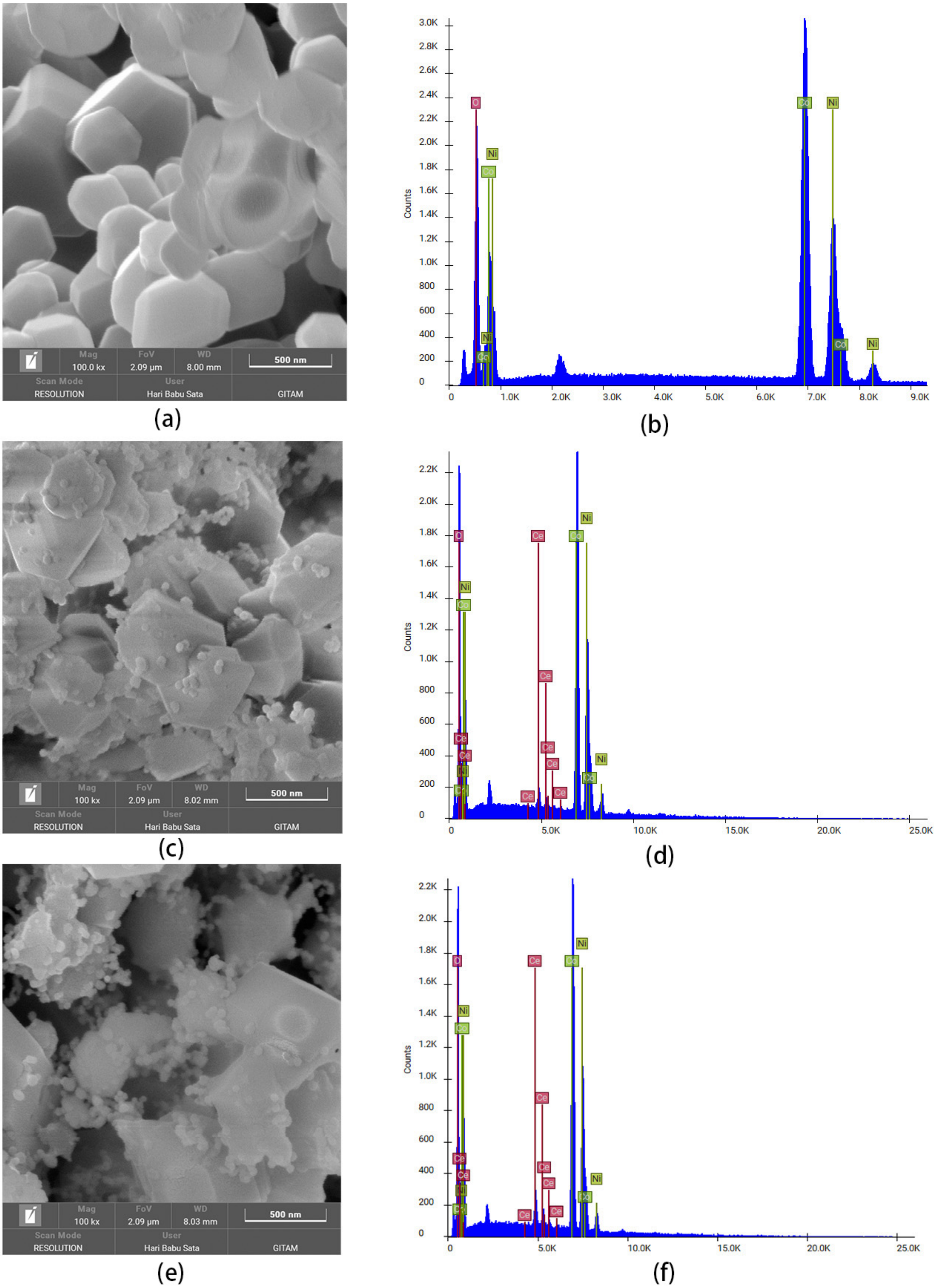

Fig. 5. SEM micrographs and EDS spectra of Ce-doped $NiCo_2O_4$ nanoparticles where (a,b) 0.00, (c,d) 0.05 and (e,f) 0.1. SEM, scanning electron microscopy; EDS, energy dispersive spectra; scale bar = 500 nm.

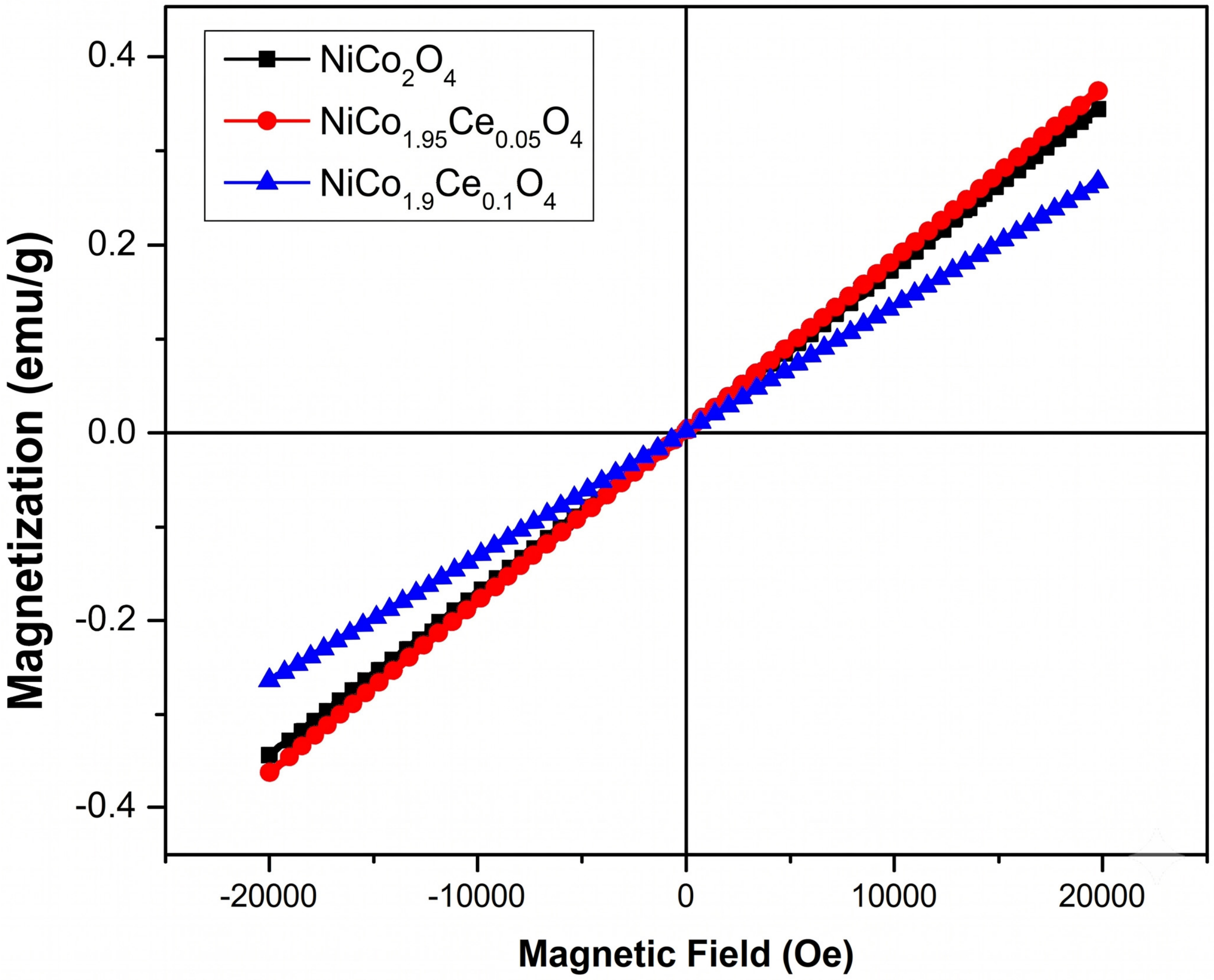

Fig. 6. Room-temperature magnetization as a function of applied magnetic field for Ce-doped $NiCo_2O_4$ spinel oxide nanopowders.

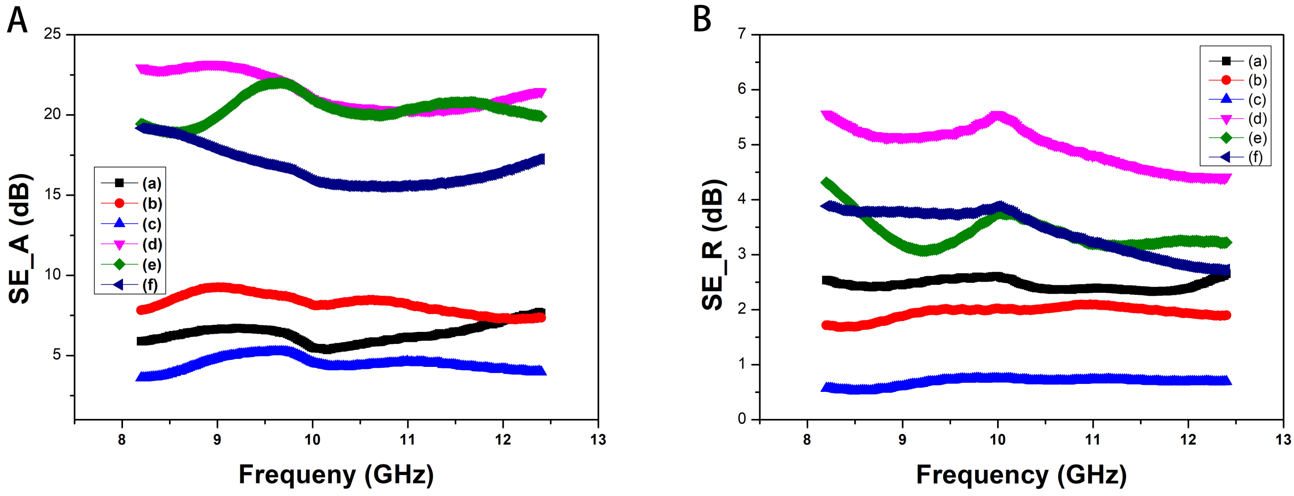

Fig. 7. EMI shielding effectiveness due to (A) absorption and (B) reflection of $NiCo_2O_4$/PVA/rGO composite films, where (a,d) x = 0.00, (b,e) 0.05 and (c,f) 0.1. EMI, electromagnetic interference; PVA, polyvinyl alcohol; rGO, reduced graphene oxide.

grain coarsening and resulting in smaller crystallite sizes (14 nm) compared to the undoped sample (36 nm).

4.2 FTIR Spectra Analysis

From the Fig. 4, the peak near 550 cm^{-1} corresponds to the stretching vibrations of Co–O bonds in tetrahedral

Table 3. Composition (x), Tetrahedral and octahedral peak positions, force constants and average grain size of Ce-doped $NiCo_2O_4$ spinel oxide nanoparticles.

Composition (x)	Vibrational band (cm^{-1})		Force constants (dyne/cm)		Avg. grain size (nm)
	Tetrahedral	Octahedral	Kt	Ko	
	υ1	υ2			
0	650	548.9	192,064	188,175	462
0.05	653.5	550.9	205,652	180,901	445
0.1	659.4	552.9	223,515	180,811	409

sites, while the peak around 600 cm^{-1} relates to Ni–O vibrations in octahedral sites of the inverse spinel lattice. This confirms the formation of the $NiCo_2O_4$ inverse spinel structure. The variation in intensity of peaks suggests that Cerium incorporation into the lattice affects the local bonding environment and may enhance the M–O linkages or increase crystallinity. The peak near 600 cm^{-1} shifts slightly toward higher wavenumbers in the doped samples. This shift can be attributed to lattice distortion caused by the replacement of Ni or Co ions with larger Ce ions, which alters bond lengths and force constants (listed in Table 3). No significant peaks indicating impurity phases are observed, suggesting that the phase purity of the doped nanoparticles. The increase in tetrahedral force constant (K_t) and wavenumber (υ_1) supports redistribution of cations toward octahedral sites, correlated with Ce ions' preference for B site occupancy.

4.3 Microscopic and Elemental Analysis

It is clear from Fig. 5 that the agglomeration in all the samples is attributed to the high surface energy of nanoparticles and magnetic interactions between particles [23]. The average grain size was estimated using Image J software V4.1 (https://imagej.net/ij/) and listed in Table 3. The average grain size decreases with an increase in cerium doping from 462 to 409 nm. This trend suggests that cerium doping effectively inhibits grain growth in $NiCo_2O_4$, possibly due to the segregation of cerium ions at the grain boundaries. The micrographs also indicate a porous microstructure feature resulting from the synthesis process. During the self-ignition of the viscous gel, the rapid decomposition of the metal nitrate precursors and citric acid fuel leads to the evolution of a substantial volume of gases. These gases escape the reaction mixture, leaving behind a highly porous and ‘fluffy’ ash structure. This combination of fine grain size, intentional agglomeration, and inherent porosity is particularly favorable for EMI shielding applications. It increases the functional surface area and adjusts the dielectric and magnetic loss mechanisms within the resulting thick film composites [3,6].

From energy dispersive spectra (EDS) spectra (Fig. 5) the undoped sample (x = 0), the atomic ratio of Ni, Co, and O was found to be approximately 14.3%, 28.6%, and 57.1%, respectively. These values are in excellent agreement with the theoretical 1:2:4 ratio expected for the $NiCo_2O_4$ inverse spinel structure. As the cerium concentration increases, a systematic variation in the elemental distribution is observed. In the x = 0.05 sample, the cerium content was detected at 0.7 At. %, while the cobalt percentage decreased to 27.9 At. %, confirming that Ce ions successfully substitute for Co within the lattice. This trend is further intensified in the x = 0.1 composition, where the cerium content reaches 1.5 At. % and the cobalt content further reduces to 27.2 At. %. Notably, the nickel and oxygen percentages remained nearly constant across all compositions, indicating that cerium preferentially replaces cobalt ions without disrupting the overall spinel framework. The absence of any extraneous peaks in the EDS spectra further confirms the high purity of the synthesized nanopowders, consistent with the phase purity observed in the XRD results.

4.4 Magnetic Properties

It is well known that $NiCo_2O_4$ spinel oxides typically exhibit nearly linear, non-saturating magnetization at room temperature without prominent hysteresis. The transformation of the magnetic state upon Ce substitution can be explained through the modification of super-exchange interactions based on Neel’s molecular field theory. In the $NiCo_2O_4$ inverse spinel structure, magnetic moments arise from the coupling between cations in the tetrahedral (A) and octahedral (B) sites. The net magnetic moment (M) is defined as $M = |M_B - M_A|$. The introduction of Ce^{3+} ions, which possess a larger ionic radius (1.01 Å), leads to their preferential occupancy of the B-sites, as confirmed by our XRD intensity ratio analysis (I_{31}/I_{220}). This occupancy forces a redistribution of the host Ni and Co ions. Since Ce^{3+} has a distinct electronic configuration compared to the transition metals it replaces, its presence weakens the A-B exchange coupling strength.

The linear M-H relationship confirms that the substitution of Ce disrupts the long-range ferrimagnetic ordering typical of nickel cobaltite. This paramagnetic or weak ferrimagnetic response is due to the mixed-valence states of Ni and Co, which create antiferromagnetic exchange interactions between tetrahedral and octahedral spinel sites, thereby suppressing long-range ferromagnetic order. Williamson-Hall analysis confirms that cerium substitution reduces the crystallite size from 36 nm to 14 nm. In the ultrafine regime (14 nm), the high surface-to-volume ratio results in a 'magnetically dead' surface layer where spins are disordered and cannot contribute to long-range magnetic ordering at room temperature. This interpretation is consistent with studies on rare-earth substituted spinels [24]. The localized 4f electrons of the rare-earth ions typically provide weaker exchange interactions than the 3d-3d coupling of transition metals, ultimately manifesting as the paramagnetic behavior observed in our M-H results. Furthermore, the coexistence of Ce^{3+} and Ce^{4+} ions, which possess larger ionic radii, facilitates their preferential occupancy of octahedral sites [8]. This occupancy induces substantial local strain and disrupts the cation ordering, effectively weakening the super-exchange interactions between the A and B sites that typically underpin ferrimagnetism. The introduction of Cerium also generates lattice disorder and oxygen vacancies, leading to the formation of isolated paramagnetic clusters and unsatisfied surface spins at grain boundaries. Consequently, these factors combine to enhance spin disorder and dilute the net magnetic moment, manifesting as decreased magnetization and an increasingly linear M-H curve at higher Cerium concentrations.

4.5 EMI Shielding Parameters

It is clear from line a in Fig. 7A that the incorporation of Ce into $NiCo_2O_4$/PVA and rGO led to a substantial enhancement in absorption-dominated EMI shielding effectiveness (SE_A) across measured range in the X band. The observed variation is ascribed to the synergistic interplay between the dielectric and magnetic components. The undoped $NiCo_2O_4$/PVA composite film exhibits a moderate absorption, typically ranging between 5 and 7 dB, primarily due to the magnetic loss and interfacial polarization associated with the spinel oxide nanoparticles dispersed in the insulating polymer matrix. Upon introducing a fractional quantity of Ce, a notable increase in SE_A was observed (up to approximately 10 dB for the $x = 0.05$ Ce composition), which can be attributed to the increased density of defects, enhanced lattice strain, and interfacial polarization. These factors are known to promote additional dielectric and magnetic loss mechanisms in the composite. Further, a dramatic improvement in absorption shielding was achieved by incorporating rGO (Fig. 7B (d,e,f)), where SE_A values reached 15–24 dB. This enhancement is ascribed to the highly conductive networks formed by rGO in the polymer matrix. In addition to the above, dielectric loss by enabling electron hopping and conductive loss pathways also optimizes impedance matching for maximized absorption.

The Ce-doped $NiCo_2O_4$ nanoparticles provide significant magnetic loss through domain wall resonance and spin relaxation. Simultaneously, the rGO sheets establish an extensive three-dimensional conductive network, enabling dielectric loss via electron hopping and ohmic dissipation. Recent studies have demonstrated that the coexistence of Ce^{3+} and Ce^{4+} ions facilitates a charge compensation mechanism, leading to the generation of oxygen vacancies within the spinel lattice [24,25,26]. These vacancies act as dipoles, significantly enhancing the interfacial polarization (Maxwell-Wagner-Sillars effect) at the high-frequency X-band. Furthermore, the localized 4f electrons of Ce^{3+} introduce a controlled disruption of the 3d–3d super-exchange coupling between Ni and Co ions, which optimizes the magnetic loss tangent. This dual-modality—where Cerium simultaneously boosts dielectric loss through defect engineering and modifies magnetic relaxation—is a primary factor in achieving the superior, absorption-dominated EMI shielding effectiveness observed in these rGO-integrated composites. Fig. 7B shows reflection shielding effectiveness (SER) values of the composite film samples. All the samples show a low reflection loss across the measured frequency range (8–12 GHz). For the $NiCo_2O_4$/PVA and Ce-doped $NiCo_2O_4$/PVA samples, SER generally lies between 1 and 3 dB due to impedance matching and relatively low surface conductivity. Further, with increasing Ce content and addition of rGO, SER slightly increases and reaching up to 5–6 dB. This marginal improvement due to enhanced charge carrier concentration and formation of secondary reflection pathways in the composite film. However, absorption remains the dominant shielding mechanism in all compositions.

4.6 Limitations

Although the present research describes a successfully synthesized massive film desert material in terms of EMI shielding performance with Ce-doped $NiCo_2O_4$/PVA/rGO composites, a few reasonable limitations should be noted. In a first step, only the EMI shielding effectiveness in a wide-band (8–12 GHz) frequency range of X-band, was examined. So far, the possible shielding abilities of these composites in other important telecommunication frequency bands (like the Ku, K or Ka bands) have not been investigated. Second, although these composite films are proposed as lightweight and flexible materials for applications, the current work does not perform a quantitative evaluation of their mechanical properties, which can include tensile strength and flexibility during repeated bending cycles, nor their stability at elevated temperature in the polymer matrix. Third, only two doping concentrations ($x = 0.05$ and $x = 0.1$) were investigated for cerium substitution. Future studies that vary the doping levels over a broader range and use systematic characterization of the composite film thickness would help to fully optimize the impedance matching, magnetic loss, and dielectric loss mechanisms for potential commercial EMI shielding applications.

5. Conclusions

In summary, Ce-doped $NiCo_2O_4$ nanopowders were successfully synthesized via a facile sol-gel auto-combustion method. XRD analysis confirmed the formation of a single-phase cubic spinel structure, while the systematic increase in lattice parameter validated the successful incorporation of Ce into the lattice. The significant enhancement in EMI shielding effectiveness, particularly in the rGO-integrated composites, is attributed to several synergistic mechanisms. The inclusion of conductive rGO creates a three-dimensional conductive network within the PVA matrix, which facilitates electron hopping and ohmic losses. Furthermore, the combined magnetic loss from the spinel filler and the dielectric loss from the rGO optimize the impedance matching, allowing for higher wave penetration and subsequent dissipation through multiple internal reflections. These results demonstrate that the Ce-doped $NiCo_2O_4$/PVA/rGO composites are lightweight and efficient candidates for high-performance absorption-dominated EMI shielding applications.

Availability of Data and Materials

The datasets used and analyzed during the current study are available from the corresponding author on reasonable request.

Author Contributions

Formal analysis and investigation [UV], Writing - original draft preparation, Methodology [RBB], Conceptualization and design of work, Supervision [KS], General Analysis [VSJ]. All authors contributed to editorial changes in the manuscript. All authors read and approved the final manuscript. All authors have participated sufficiently in the work and agreed to be accountable for all aspects of the work.

Ethics Approval and Consent to Participate

Not applicable.

Acknowledgment

We thank the support from Department of Physics, Andhra University and management of Gayatri Vidya Parishad College of Engineering for women.

Funding

This research received no external funding.

Conflicts of Interest

The authors declare no conflicts of interest.

Declaration of AI and AI-Assisted Technologies in the Writing Process

The Gemini was only used to correct the grammatical errors, not for writing the manuscript. The manuscript and results are studied and analyzed and written by all authors. Only to correct the grammar, we have taken the help of a free AI tool. After using this tool, the authors reviewed and edited the content as needed and take full responsibility for the content of the publication.

References

[1] Kumar S, Tahira A, Bhatti AL, Bhatti MA, Mari RH, Shaikh NM, et al. Transforming $NiCo_2O_4$ nanorods into nanoparticles using citrus lemon juice enhancing electrochemical properties for asymmetric supercapacitor and water oxidation. RSC Advances. 2023; 13: 18614–18626. https://doi.org/10.1039/d3ra02438e

[2] He X, Dong Y, Yin F, Li G, Zhao X. $NiCo_2O_4$ nanoparticles rich in oxygen vacancies: Salt-Assisted preparation and boosted water splitting. Frontiers in Chemistry. 2022; 10: 996084. https://doi.org/10.3389/fchem.2022.996084

[3] Kershi RM, Alshehri AM, Attiyah RM. Enhancement of Ni-Zn ferrite nanoparticles parameters via cerium element for optoelectronic and energy applications. Discover Nano. 2023; 18: 139. https://doi.org/10.1186/s11671-023-03921-6

[4] Mao Z, Zhang J, Tu T, Li X, Ji J, Yang P, et al. Cerium driven active site relocation in spinel Co_3O_4 enables stable chlorine evolution in acidic media. Nature Communications. 2026; 17: 3763. https://doi.org/10.1038/s41467-026-70443-x

[5] Almousawi M, Aridi A, El Sayed MY, Abdallah AM, Labban W, Habchi R, et al. Synthesis, structural characterization, and magnetic properties of Ce and Sb doped Co-Ni-Cd-Cu ferrite nanoparticles. Physica B: Condensed Matter. 2025; 715: 417591. https://doi.org/10.1016/j.physb.2025.417591

[6] Zeng X, Liu J, Chu K, He J, Zhang J, Zhu H, et al. Atomic-level cation occupation and magnetic properties of Ce^{3+}-doped $ZnFe_2O_4$ spinel ferrite. RSC Advances. 2025; 15: 20908–20915. https://doi.org/10.1039/d5ra01515d

[7] Hashim M, Kumar S, Koo BH, Shirsath SE, Mohammed EM, Shah J, et al. Structural, electrical and magnetic properties of Co–Cu ferrite nanoparticles. Journal of Alloys and Compounds. 2012; 518: 11–18. http://doi.org/10.1016/j.jallcom.2011.12.017

[8] Padalia D, Johri UC, Zaidi MG. Effect of cerium substitution on structural and magnetic properties of magnetite nanoparticles. Materials Chemistry and Physics. 2016; 169: 89–95. http://doi.org/10.1016/j.matchemphys.2015.11.034

[9] Ullah I, Khan Q, Ahmad R, Ahamd I, Khan I. Effect of cerium doping on the structure, magnetic, electric and dielectric properties of spinel nano-magnets Mn0. 5Zn0. 5Fe2O4. Applied Physics A. 2024; 130: 603. https://doi.org/10.1007/s00339-024-07769-0

[10] Asif RM, Aziz A, Akhtar MN, Khan MA, Abbasi MN, Abdul Muqeet H. Synthesis and characterization of cerium doped NiZn nano ferrites as substrate material for multi band MIMO antenna. PloS One. 2024; 19: e0305060. https://doi.org/10.1371/journal.pone.0305060

[11] Mashadi M, Suyanti S, Setiawan J, Yunasfi Y, Adi WA. Magnetic and microwave absorbing properties of cerium substituted zinc ferrite synthesized using milling technique. Journal of Superconductivity and Novel Magnetism. 2023; 36: 721–731. https://doi.org/10.1007/s10948-023-06518-3

[12] Iqbal N, Anastasiou A, Aslam Z, Raif EM, Do T, Giannoudis PV, et al. Interrelationships between the structural, spectroscopic, and antibacterial properties of nanoscale (< 50 nm) cerium oxides. Scientific Reports. 2021; 11: 20875. https://doi.org/10.1038/s41598-021-00222-9

[13] Rani P, Jyothirmai E, Ludhiya V, Prasad KV, Pandari J. Novel low sintering studies on structural, optical, magnetic and electrical properties of rare earth ’Ce’doped composite Ni-Zn nano ferrites. Materials Chemistry and Physics: Sustainability and Energy. 2025; 2: 100004. https://doi.org/10.1016/j.macse.2024.100004

[14] Nguyen NV, Tran TV, Luong ST, Pham TM, Nguyen KV, Vu TD, et al. Facile synthesis of a NiCo2O4 nanoparticles mesoporous carbon composite as electrode materials for supercapac-

itor. ChemistrySelect. 2020; 5: 7060–7068. https://doi.org/10.1002/slct.202001410

[15] Li Y, Cheng H, Zhang J, Fu Y. Ce doping-boosted lattice oxygen activation for NiCo2O4 in acidic oxygen evolution reaction. Applied Surface Science. 2026; 717: 164784. https://doi.org/10.1016/j.apsusc.2025.164784

[16] Kaur M, Chand P, Anand H. Facile synthesis of NiCo2O4 nanostructure with enhanced electrochemical performance for supercapacitor application. Chemical Physics Letters. 2022; 786: 139181. https://doi.org/10.1016/j.cplett.2021.139181

[17] Priyadharshini P, Pushpanathan K. Synthesis of Ce-doped NiFe2O4 nanoparticles and their structural, optical, and magnetic properties. Chemical Physics Impact. 2023; 6: 100201. https://doi.org/10.1016/j.chphi.2023.100201

[18] Razik NA. Precise lattice constants determination of cubic crystals from x-ray powder diffractometric measurements. Applied Physics A. 1985; 37: 187–189. https://doi.org/10.1007/BF00617505

[19] Muniz FTL, Miranda MAR, Morilla Dos Santos C, Sasaki JM. The Scherrer equation and the dynamical theory of X-ray diffraction. Acta Crystallographica. Section A, Foundations and Advances. 2016; 72: 385–390. https://doi.org/10.1107/S205327331600365X

[20] Kibasomba PM, Dhlamini S, Maaza M, Liu CP, Rashad MM, Rayan DA, et al. Strain and grain size of TiO2 nanoparticles from TEM, Raman spectroscopy and XRD: The revisiting of the Williamson-Hall plot method. Results in Physics. 2018; 9: 628–635. https://doi.org/10.1016/j.rinp.2018.03.008

[21] Grimes NW, Collett AJ. Infrared absorption spectra of ferrites. Nature physical science. 1971; 230: 158. https://doi.org/10.1038/physci230158a0

[22] Lai D, Chen X, Liu X, Wang Y. Flexible Poly (vinyl alcohol)/reduced graphene oxide coated carbon composites for electromagnetic interference shielding. ACS Applied Nano Materials. 2018; 1: 5854–5864. https://doi.org/10.1021/acsanm.8b01499

[23] Ansari MA, Akhtar S, Rauf MA, Alomary MN, AlYahya S, Alghamdi S, et al. Sol-Gel Synthesis of Dy-Substituted $Ni_{0.4}Cu_{0.2}Zn_{0.4}(Fe_{2-x}Dy_x)O_4$ Nano Spinel Ferrites and Evaluation of Their Antibacterial, Antifungal, Antibiofilm and Anticancer Potentialities for Biomedical Application. International Journal of Nanomedicine. 2021; 16: 5633–5650. https://doi.org/10.2147/IJN.S316471

[24] Li DS, Wang SJ, Zhou Y, Jiang L. Lightweight and hydrophobic Ni/GO/PVA composite aerogels for ultrahigh performance electromagnetic interference shielding. Nanotechnology Reviews. 2022; 11: 1722–1732. https://doi.org/10.1515/ntrev-2022-0088

[25] Pubby K, Babu KV, Narang SB. Magnetic, elastic, dielectric, microwave absorption and optical characterization of cobalt-substituted nickel spinel ferrites. Materials Science and Engineering: B. 2020; 255: 114513.

[26] Rajenimbalkar RS, Deshmukh VJ, Patankar KK, Somvanshi SB. Effect of multivalent ion doping on magnetic, electrical, and dielectric properties of nickel ferrite nanoparticles. Scientific Reports. 2024; 14: 29547. https://doi.org/10.1038/s41598-024-81222-3